Chapter IV

Software Integrated Electrochemical Sensing Platform for the Detection of Creatinine

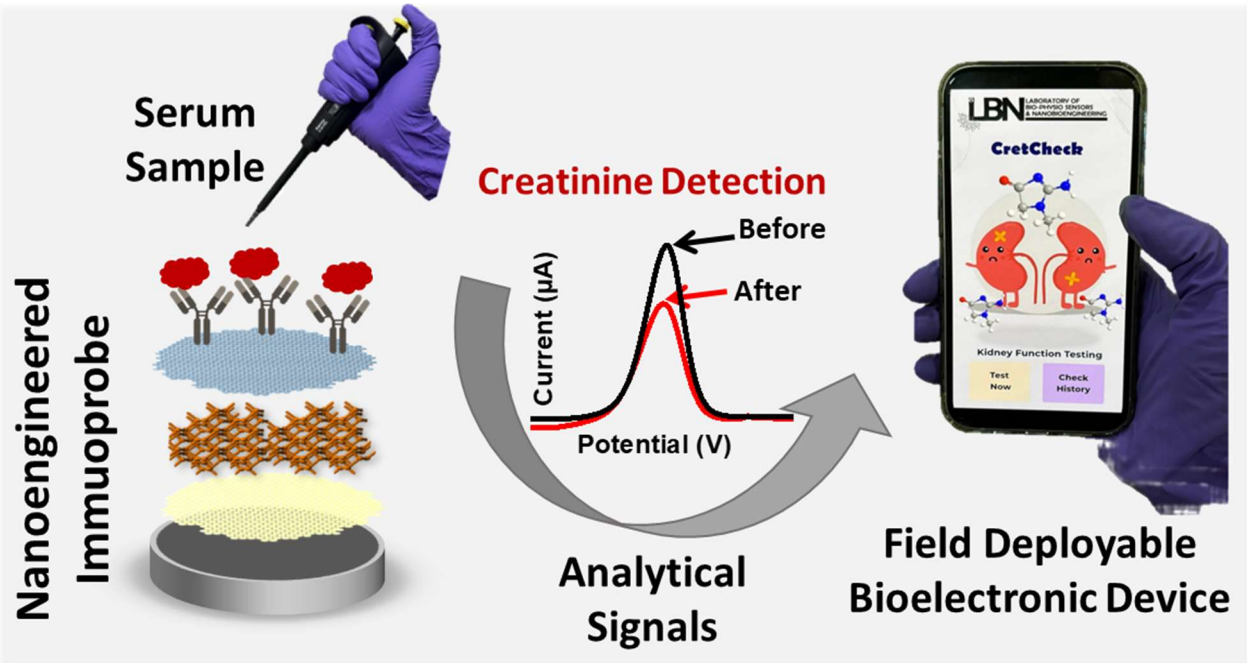

Divya *et. al*, *ACS Biomaterial Science and Engg., 2024, Vol 10, 6603–6614*

ACS Publications
Most Trusted. Most Cited. Most Read.

ACS Biomaterials
SCIENCE & ENGINEERING

1. Introduction

Millions of people worldwide suffer from chronic kidney disease (CKD), which is a major global health burden and offers enormous challenges to healthcare systems [1]. The global burden of disease research 2017 estimated the contribution of 354 illnesses and injuries as well as 84 risk factors to morbidity and mortality between 1990 and 2017 [2]. It was reported that there is a surge in morbidity and mortality at the national, regional, and worldwide levels due to CKD and reduced kidney function. To emphasize and garner attention on CKD, an initiative had been started which termed CKD as "Common, Harmful, and Treatable" [3]. It affects more than 10% of the global population and it is reported that it will become 5th major cause of mortalities by 2040 [4,5]. Furthermore, it becomes crucial to diagnose and treat CKD promptly in order to meet the 2030 UN Sustainable Development Goal of lowering the effect of communicable diseases to one-third. Therefore, to diagnose the renal disease, it is required to develop methods for monitoring the levels of related biomarkers. Creatinine is a byproduct produced due to breakdown of creatine which is an essential component of muscles. Generally, creatinine is eliminated from the blood by the kidney and is considered as a key biomarker for diagnosing, tracking, and treatment of CKD [6,7]. Its accurate and timely identification is thus essential for prompt intervention and successful disease management [8,9].

The conventional methods for the detection of creatinine are colorimetry, enzymatic assays, spectrophotometry, high pressure liquid chromatography, mass spectroscopy, capillary zone electrophoresis, flow injection analysis systems, and nuclear magnetic resonance [10–13]. These methods are frequently constrained by their intricate instrumentation, lengthy processing periods, and vulnerability to interference from other substances in biological samples. As a result, there has been a surge in interest for creating novel biosensing technologies that can get past these obstacles

and transform the diagnosis industry [14,15]. The recent developments in the field of nanotechnology, material synthesis, and biorecognition components lead to novel sensing technologies with unmatched sensitivity, specificity, and speed of analysis [16]. These biosensors improve signal transduction and detection limits by taking advantage of the unique qualities of nanomaterials, such as high surface area-to-volume ratios, excellent conductivity, robustness, and biocompatibility [17,18]. Apart from their analytical capabilities, biosensors exhibit great potential for point-of-care applications, as they can facilitate the real-time, remote monitoring of target without the need of sophisticated instrument and skilled personnel. Therefore, the incorporation of biosensors into the arsenal for creatinine detection has great potential to improve CKD diagnosis by enabling quick, affordable, and easy detection outside centralized laboratories. Electrochemical biosensors have become one of the preferred choices for creatinine detection in recent years. Recently in this direction numerous studies have been reported for the electrochemical detection by incorporating Cu-MOF [19], copper over polymelamine formaldehyde [20], Cu_2O-Au nanohybrid [21], cobalt with methylhydantoin [22], nanoporous gold [23], carbon nanotubes/folic acid/silver nanoparticles [24] etc. Although these methods are able to detect the creatinine, but they may suffer due to false positive signals when tested in various body fluids due to metal-based interactions [19,21]. Not only this, these methods also require multi-steps in data analysis to obtain the results, limiting their deployment for bed-side analysis. Therefore, there is need of a simpler, highly selective, and field deployable analytical device that can cater these limitations. This can be achieved by grafting a selective receptor onto a highly conducting surface for signal generation and further integrating it with a personalised device module.

In this study, we have tried to incorporate the unexplored boron-doped MXene (BMX) for the development of electrochemical immunosensor for creatinine detection. Since the discovery of

MXenes in 2011, they have been widely in use as an innovative kind of two-dimensional materials for various potential applications because of their favourable inherent qualities, including large specific surface area, outstanding hydrophilicity, high chemical stability, great thermal and electrical conductivity, and environmental friendliness [25,26]. They have been effectively utilized in biomedical applications, composite materials, electromagnetic shielding, sensors, hydrogen storage, energy storage (rechargeable batteries, supercapacitors, photo/electrocatalysis, solar cells), and environmental remediation (water treatment, heavy metal adsorption) [27,28]. Despite their great potential, MXenes are quite prone to performance deterioration. The restacking of the layers, oxidation susceptibility, limited flexibility, and high contact resistance are some of the main obstacles encountered in MXene research [29]. Doping or addition of foreign materials within the layers prove to be an efficient technique for modulating the chemical and physical characteristics of such two-dimensional materials [30]. Element doping contributes to increasing the material's conductivity by converting inert sites into electrochemically active species [31]. Because of this, they can transmit electrons quickly, which makes them excellent choices as transducers in biosensing applications. Therefore, we hypothesize BMX may enhance conductivity and help in improved signal generation of the developed sensor.

In addition, we have indigenously developed a smartphone-integrated deployable system for the sensitive detection of creatinine in serum sample within clinically relevant ranges. The sensor platform was at first fabricated using nanocomposites comprising BMX, gold nanoparticles (AuNPs), and polyaniline (PANI). Then, anti-creatinine (Anti-Cret) antibodies were immobilized on the nanocomposite surface using a bioconjugation reaction for the specific detection of creatinine. The synthesized material and subsequent modifications on electrode surface with each step were characterized by both physical and electrochemical techniques. The analytical signals at

varying concentrations of creatinine in buffer and serum matrices were recorded using differential pulse voltammetry (DPV). To ease the process of data analysis and its bedside deployment, a software assisted device was developed that enables a user-friendly data interpretation. This system can help in easy and affordable testing of creatinine in primary health care centres.

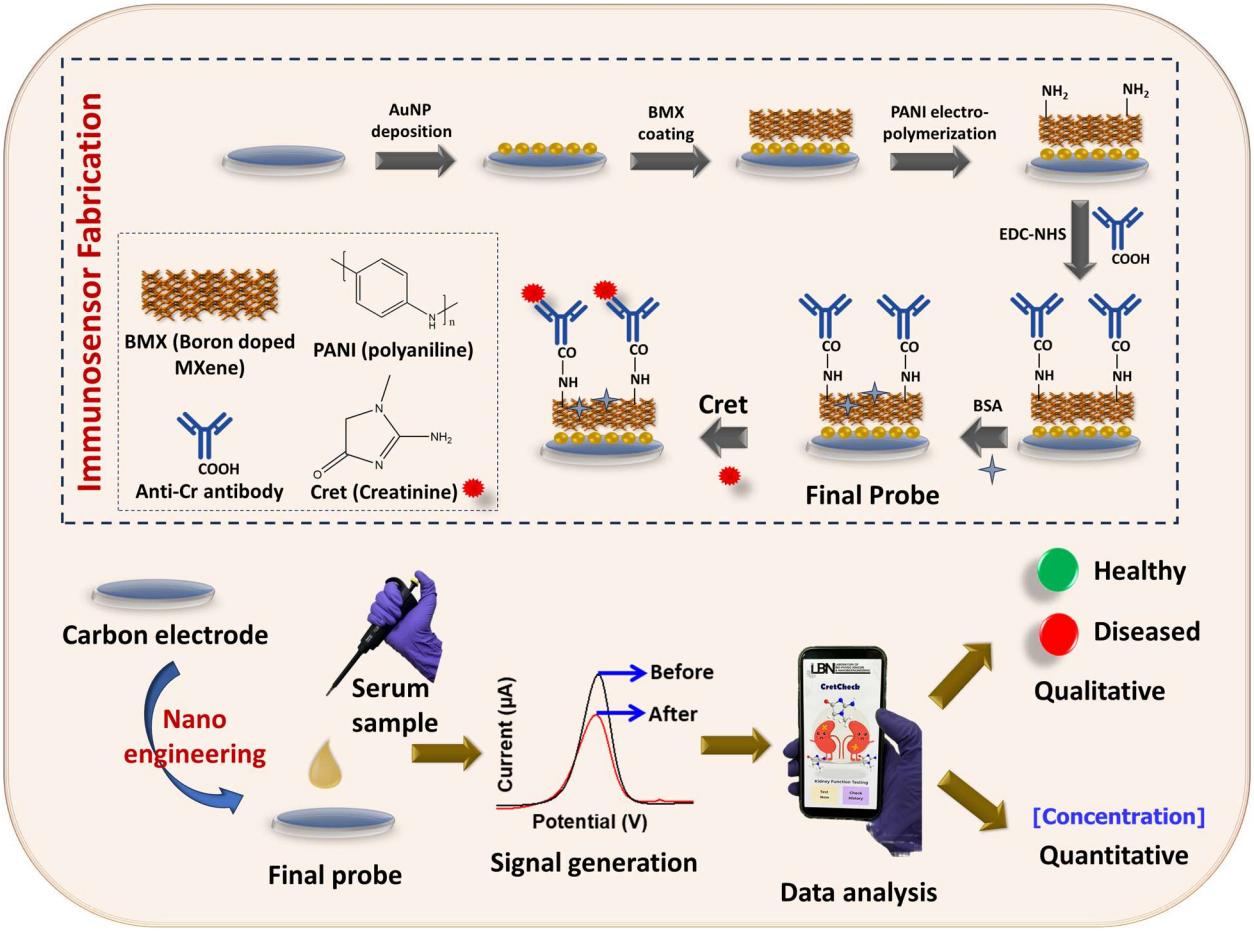

Figure 4.1: *Schematic representation of the step-by-step fabrication of immunosensor and its integration with smartphone device*

2. Experimental Section

2.1 Material and Methods

The reagents and chemicals utilised were of analytical grade. Hexaammineruthenium(III) chloride (RuHex), bovine serum albumin (BSA), and aniline were purchased from Himedia Pvt. Ltd. (Mumbai, India). Anti-Cret antibody (ab30719) was procured from Abcam, Inc., Cambridge, UK.

Titanium aluminium carbide (Ti_3AlC_2) was purchased from Sigma-Aldrich (St. Louis, Unites States). Hydrofluoric acid (HF) was procured from Fischer Scientific (Hampton, United States). Standard serum (RM1112) was procured from Himedia Pvt. Ltd. (Mumbai, India). Creatinine, 1-(3 dimethylaminopropyl) 3-ethyl carbodiimide hydrochloride (EDC), n-hydroxysuccinimide (NHS), sodium monophosphate, sodium bisphosphate, chloroauric acid ($HAuCl_4$), sodium chloride, serum albumin, lactose, ascorbic acid, uric acid, ribonuclease, glutathione and potassium chloride were procured from SRL Pvt. Ltd. (Mumbai, India). Boric acid was procured from SD fine-chem ltd. (Mumbai, India). EDC/NHS was prepared in 0.1 M PBS. Double distilled water from a Milli-Q purifier was used to prepare solutions. A potentiostat (Palm Sense BV, Houten, The Netherlands) consisting of platinum wire, carbon electrode, and silver/silver chloride as auxiliary, working, and reference electrode, respectively was used for electrochemical analysis.

2.2 Instrumentation

SEM (scanning electron microscope) (EVO - Scanning Electron Microscope MA15/18, CARL ZEISS MICROSCOPY LTD., Oxford Instruments Nanoanalysis) was used for morphological studies. EDS (energy dispersive X-ray spectroscopy) (Team Pegasus Integrated EDS-EBSD with Octane Plus and Hikari Pro, EDAX Inc.) was used for elemental analysis. SPM (scanning probe microscopy) (NTEGRA Prima, NT-MDT Service & Logistics Ltd.) was employed to monitor the topographical changes after each fabrication step. Using Nova Px Software, 3D images and micrograph assessment of the modified surface was carried out for each of the subsequent steps. Fourier Transform Infrared Spectroscopy (FTIR) (Nicolet iS5, THERMO Electron Scientific Instruments LLC) was used for determining the functional groups present in every modified surface.

2.3 Synthesis of boron-doped MXene (BMX)

Using a slightly modified version of the selective etching method, 2D Ti_3C_2-MXene was prepared by removing the aluminium layer from bulk Ti_3AlC_2 [32]. In brief, 20 mL of 40% HF was mixed with 1 g of Ti_3AlC_2 powder, and the mixture was constantly agitated for 24 hours at room temperature. After the HF treatment, the solution was centrifuged and washed with ultrapure water until the pH reached 6-7. Following a 12-hour drying process at 80 °C, the sample was put into a desiccator and kept at ambient temperature for further use. In order to synthesise boron-doped Ti_3C_2-MXene further, 80 mg of the produced Ti_3C_2-MXene was dissolved in 40 mL of water and mixed with boric acid (3 mg/mL) for 30 min at room temperature. The mixture was subsequently put into a Teflon-lined autoclave reactor and heated at 180 °C for 12 hours. The sample was washed with ultrapure water using centrifuge. The final product was dried at 80 °C and stored in desiccator.

2.4 Fabrication of Immunosensor

The sensor probe was fabricated by sequential surface modifications on bare glassy carbon electrode (GCE). A detail procedure of sensor fabrication, signal generation, and data analysis have been shown in **Figure 4.1**. In the first step, the GCE surface was modified with electrochemical deposition of AuNPs. In this step, the AuNPs were deposited by running linear sweep voltammetry (LSV) at -0.6 V for 60 s for three consecutive scans from 1.5 V - 0.4 V in acidic solution of $HAuCl_4$ (0.001% in 0.5 M H_2SO_4) with the scan rate of 100 mV/s. In the next step, BMX was coated on the GCE/AuNP modified surface and allowed to dry for 10 min at room temperature to form GCE/AuNP/BMX surface. Further, the modified surface was scanned using CV in 0.1 mol/L aniline in 0.5 M H_2SO_4 from 0.0 - 1.0 V potential window for 10 cycles with a scan rate of 100 mV/s for the coating of PANI [33]. Subsequently, the creatinine antibody was activated by mixing the optimized concentration of antibody with freshly prepared EDC-NHS (100 mM: 100 mM) for

10 min at room temperature. Then the mixed sample was allowed to react with the modified surface (GCE/AuNP/BMX/PANI) and incubated at ambient temperature. The antibody-modified surface (GCE/AuNP/BMX/PANI/Anti-Cret) was rinsed with PBS buffer to remove any unbound molecule on the surface. Finally, to prevent any non-specific binding the sensing surface was blocked using 5 µL of 0.1 % BSA to obtain the final sensing probe. The developed surface was rinsed with 0.1 M PBS buffer (pH-7.2) and used for further experimentation.

2.5 Electrochemical Measurements

Measurements of cyclic voltammetry (CV) and electrochemical impedance spectroscopy (EIS) were performed in an electrochemical cell containing 5.0 mM RuHex. CV was performed at 50 mV/s in the potential window between -0.6 and 0.4 V. A 10 mV amplitude alternating wave was used for the EIS experiments using the frequency from 10,000 - 0.05 Hz. The PS Trace software (PalmSens 4) was used to correlate the impedance values to an equivalent Randles circuit simulation. The results were consistent with the Randles model. The analytical performance of the developed sensing probe was studied using DPV in the potential window between -0.6 and 0.2 V with a scan rate of 20 mV/s.

3. Results and Discussion

3.1 Characterization of synthesized BMX

The morphological structure and elemental mapping of the synthesized BMX were first investigated using SEM and EDS. The successful formation of BMX multi-layered structure was confirmed by the SEM images, which showed a sheet-like structure consisting of numerous layers (**Figure 4.2(a-b)**). The multi-layered structure of BMX could increase the effective surface area and thus could enhance electrochemical performance. After this, elemental mapping and EDS analysis were performed to validate boron doping and MXene's elemental composition. The EDS

spectrum of the BMX is shown in **Figure 4.2(c)** and the constituent elements B, C, O, F and Ti were found in the atomic percentages of 13.65%, 11.21%, 35.21%, 1.46%, and 38.47%, respectively. The elemental mapping results are shown in **Figure 4.2(d)** as merged micrograph of all elements. The individual elements i.e., B, C, O, F, and Ti have been demonstrated using red, dark green, light green, yellow, and purple-coloured patterns, respectively (**Figure 4.2(e-i)).** This verified that all the elements are present and uniformly distributed. Consequently, the morphology and chemical content of the doped MXene were confirmed by SEM-EDS evaluations.

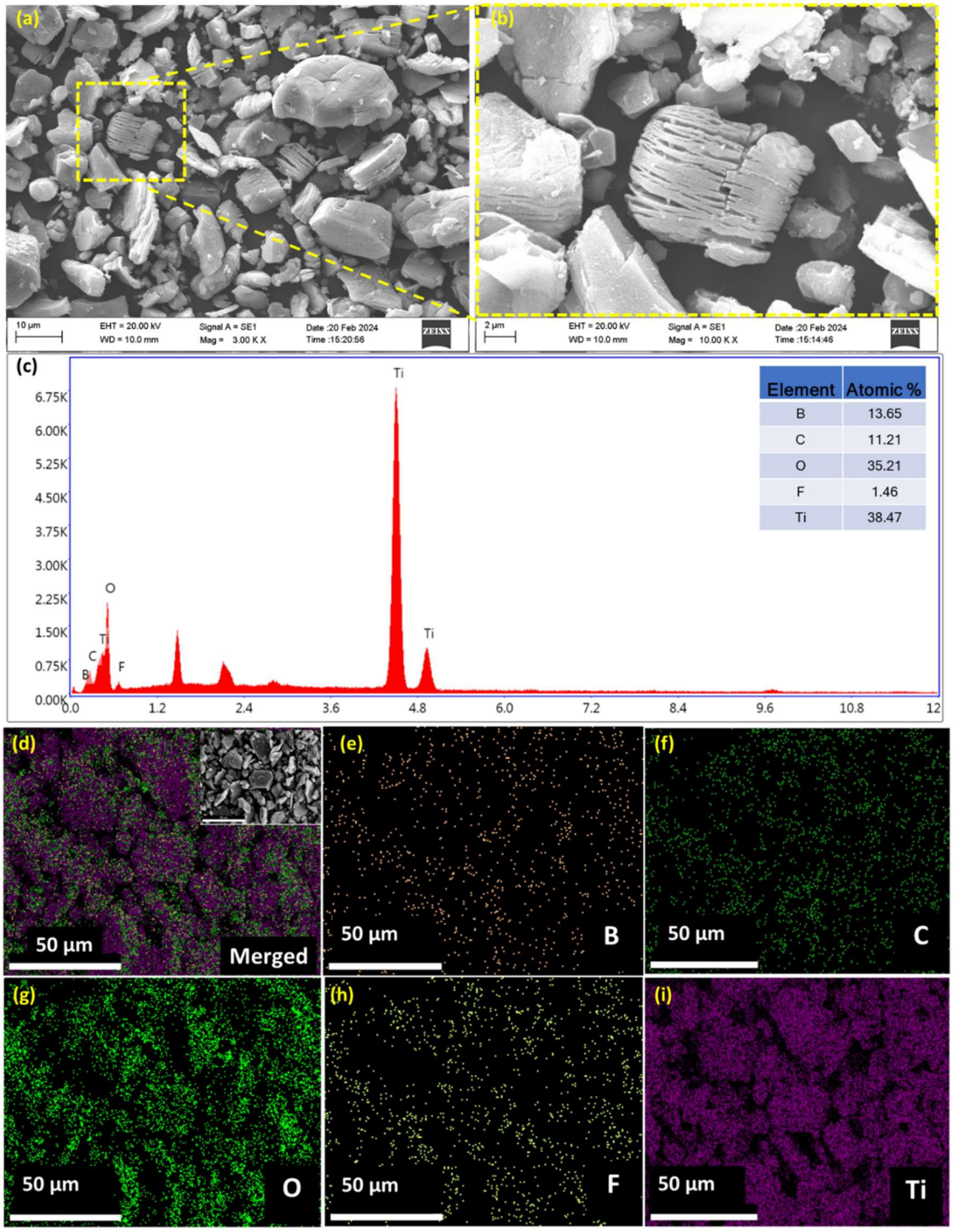

Figure 4.2: ***(a)*** *SEM images of synthesized Boron-doped MXene at 10 µm, and enlarged image at* ***(b)*** *2 µm;* ***(c)*** *EDS spectrum of BMX (inset: table representing the atomic % of every element);* ***(d)*** *Merged elemental mapping showing all the elements present in BMX (inset: SEM image of mapped area)* ***(e)*** *boron (red);* ***(f)*** *carbon (dark green);* ***(g)*** *oxygen (light green);* ***(h)*** *fluorine (yellow);* ***(i)*** *titanium (purple) distribution in the structure (brightness +40%, contrast – 40%)*

3.2 Surface Characterization of the fabricated sensor

After confirming the successful synthesis of BMX, the sequentially modified electrode surface was characterised using SPM to observe the structural changes. 3D images and respective 2D micrographs representing the corresponding changes after each step along with mathematical surface topographical parameter like z-deflection values are shown in **Figure 4.3**. At first step, z-deflection of the bare electrode surface was found to be 0.97 nm (**Figure 4.3(a)**). This also represented surface uniformity due to no surface modification on the electrode. After AuNPs deposition, the surface topology changed showing the broader crests and troughs due to the spherical nature of the AuNPs. The observed z-deflection in this case increased to 24.7 nm (**Figure 4.3(b)**), confirming the deposition of AuNPs. After BMX coating, the z-deflection value reached 75.7 nm (**Figure 4.3(c)**), which was approximately 75 times higher compared to blank surface. In this case, the surface depicts uniform patterns due to the even distribution of BMX layers and represents homogeneous distribution of crests throughout the surface. In the next step, a highly patterned surface topology was observed after PANI coating, which was completely different from the previous ones and the observed z-deflection value was 145.4 nm (**Figure 4.3(d)**). Finally, the observed z-deflection value was 209.9 nm after Anti-Cret immobilization (**Figure 4.3(e)**), which was more than 200 times higher in comparison to the bare surface. These results confirmed the changes in the surface modification with each step.

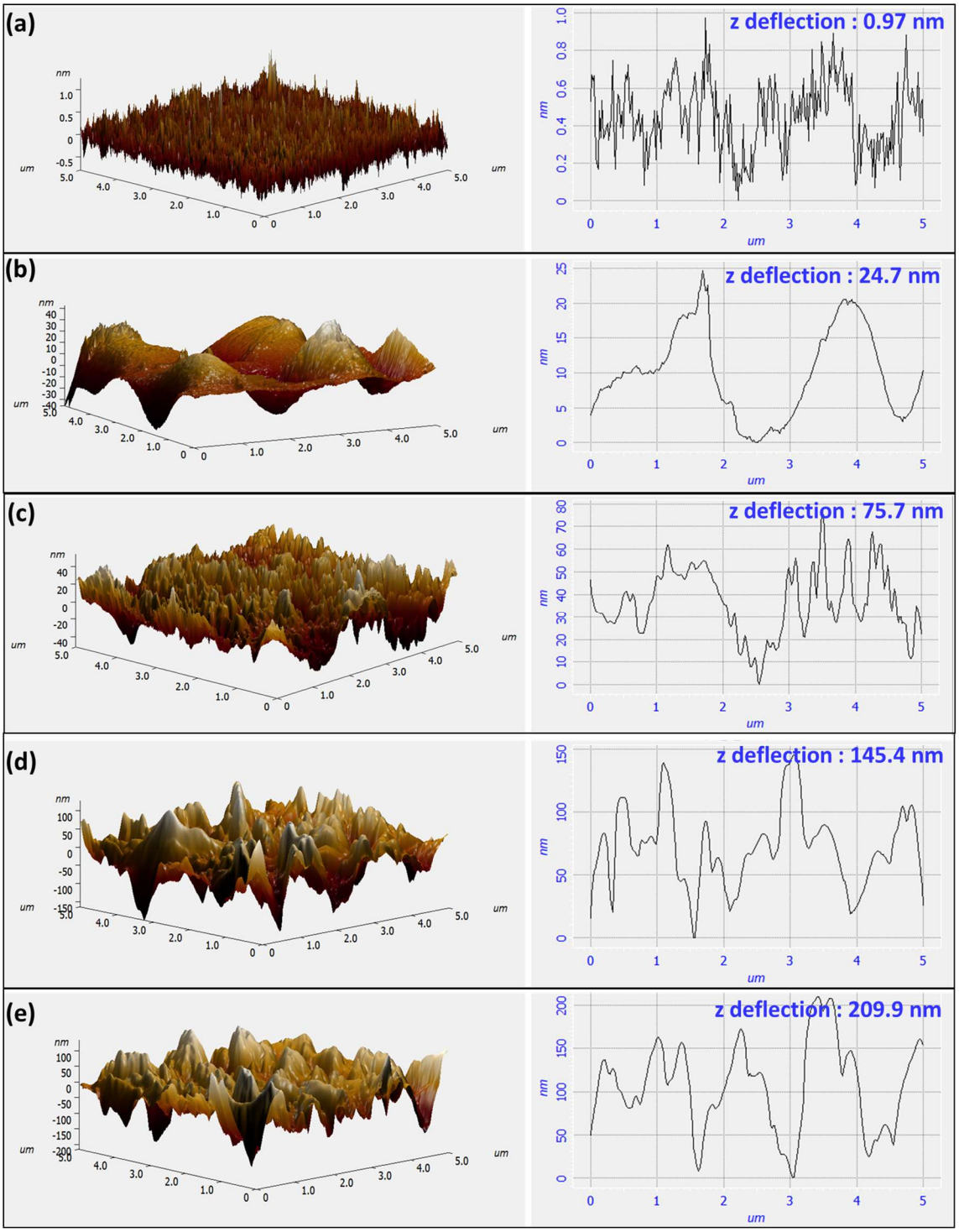

Figure 4.3: *SPM 3-D images and 2-D micrograph representing z-deflection for* ***(a)*** *bare electrode (z-deflection: 0.97 nm),* ***(b)*** *AuNP layered (z-deflection: 24.7 nm,* ***(c)*** *AuNP/BMX (z-deflection: 75.7 nm),* ***(d)*** *AuNP/BMX/PANI (z-deflection: 145.4 nm), and* ***(e)*** *AuNP/BMX/PANI/Anti-Cret* final probe *(z-deflection: 209.9 nm) surfaces*

After confirming the surface topology of the sensor probe using SPM, FTIR was further performed to analyse the chemical groups present and to observe changes in bond formation after every modification on electrode surface. **Figure 4.4** represents the FTIR spectra of the synthesized (i) BMX (black), (ii) BMX/PANI (red), (iii) BMX/PANI/Anti-Cret (blue). The peak observed for BMX at 664 cm^{-1} corresponds to C–Ti peaks (**Figure 4.4(a)**). In the next step, the additional peaks at 1538, 1496, 1307, 1247, and 875 cm^{-1} are the characteristic peaks of PANI (**Figure 4.4(b)**). The peaks at 1538 cm^{-1} and 1496 cm^{-1} correspond to C=C stretching vibrations of quinoid and benzenoid ring structures present in its chemical configuration, respectively. The peaks observed at 1307 cm^{-1} and 1247 cm^{-1} represent the C–N stretching of the ring structures present in the backbone chain. In addition, peaks observed at 875 cm^{-1} and 3382 cm^{-1} show the C–H out of plane bending vibration and N–H vibration, respectively. In the subsequent step after antibody immobilization, the additional broader peak was observed at 3296 cm^{-1} represents the –OH group present in the backbone of the antibody structure (**Figure 4.4(c)**). Not only this, the representative peaks of amide I (C=O) and amide II (N–H) bonds due to the antibody immobilization were observed at 1633 and 1531cm^{-1}, respectively. These results represent successful immobilization of antibody on the sensor probe to form final GCE/AuNP/BMX/PANI/Anti-Cret surface.

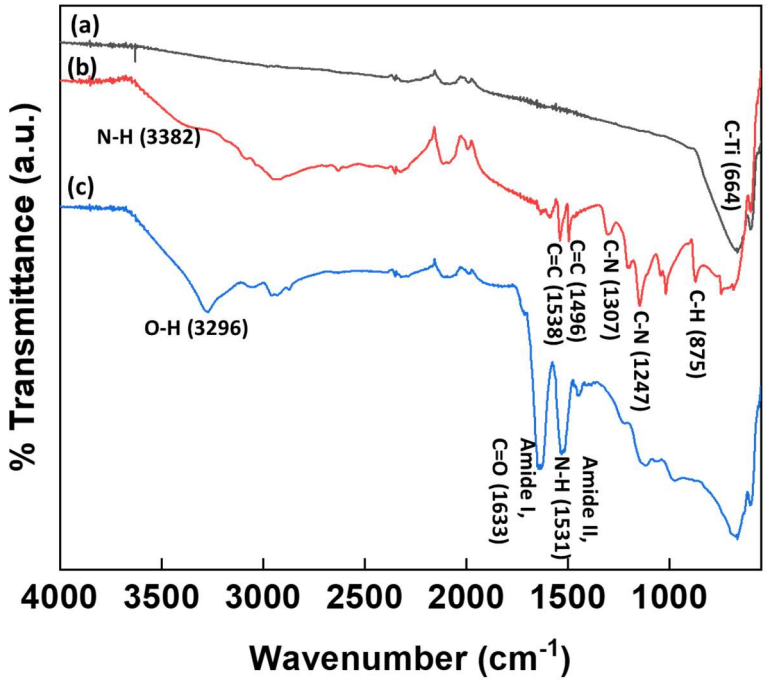

Figure 4.4: *FTIR spectra of modified surfaces* ***(a)*** *BMX,* ***(b)*** *BMX/PANI,* ***(c)*** *BMX/PANI/Anti-Cret*

3.3 Electrochemical characterization of the fabricated sensor

CV response after every modification step is represented in **Figure 4.5(a).** Initially the bare GCE signal was measured in 0.1 M PBS containing RuHex (5 mM) within the potential range of -0.6 to 0.4 V at a scan rate of 50 mV/s and a typical voltammogram was obtained due to redox reaction of RuHex (black curve). In the next step, the deposition of AuNPs was carried out using the LSV technique. The modified surface i.e. GCE/AuNP showed increased signal due to improved conductivity because of the presence of AuNPs (red curve). In the subsequent step, the synthesized BMX was coated and the increase in CV signal was observed (blue curve). This was attributed to enhanced charge transfer probably due to the increased surface area and conducting behaviour of BMX. In the next step, PANI was chosen for the antibody immobilization due to its low cost, high conductivity, and excellent biocompatibility. After PANI deposition on the electrode surface

(GCE/AuNP/BMX), the CV curve showed further increment in the peak current (green curve). This increase in the peak current of the redox probe from GCE/AuNP/BMX/PANI modified surface was due to the conductivity of PANI which enhances the electron transfer rate. The immobilization of Anti-Cret antibodies on the modified surface resulted in the generation of GCE/AuNP/BMX/PANI/Anti-Cret final probe. This demonstrated a noticeably lower peak current, due to the insulating behaviour of antibody molecules (purple curve). In the next step, when creatinine was added, further decrement in the signal response was observed, confirming the Anti-Cret and creatinine binding over the final surface (yellow curve). The anodic and cathodic peak current of the obtained CV curves after each modification step are plotted in histogram as shown in **Figure 4.5(b)**. We validated these results by performing the complimentary analysis using EIS to determine the charge transfer resistance (Rct) for each modified surface.

Figure 4.5(c) displays the Nyquist plots of the impedance spectra that were obtained from each modified surfaces in 0.1 M PBS containing 5.0 mM RuHex. The dielectric characteristics at the electrolyte/electrode interface are indicated by the value of the R_{ct}. The change in the R_{ct} were used to evaluate the interfacial characteristics on the electrode surface. The impedance spectra corresponding to the bare GCE (black), GCE/AuNP (red), GCE/AuNP/BMX (blue), GCE/AuNP/BMX/PANI (green), GCE/AuNP/BMX/PANI/Anti-Cret (purple), and GCE/AuNP/BMX/PANI/Anti-Cret/Cret (yellow) were fitted into Randles equivalent circuit (inset of Figure 5c). The obtained R_{ct} values for subsequent modified surfaces were found to be 7283 (±102) **Ω**, 6306 (±87) **Ω**, 5765 (±92) **Ω**, 4869 (±143) **Ω**, 6440 (±138) **Ω**, 6896 (±129) **Ω** respectively. The data obtained has been comprehensively shown in histogram in **Figure 4.5(d)**. The sequential decrease in the R_{ct} after AuNPs, BMX and PANI modification were observed due to the conducting behaviour of coated materials. Following the conjugation of the Anti-Cret

antibody and its interaction with Cret, a noticeable rise in the R_{ct} value was observed. The pattern of signals observed for each layer complimented in CV and EIS, not only proves its successful fabrication but also the immunocomplexation ability of the sensor.

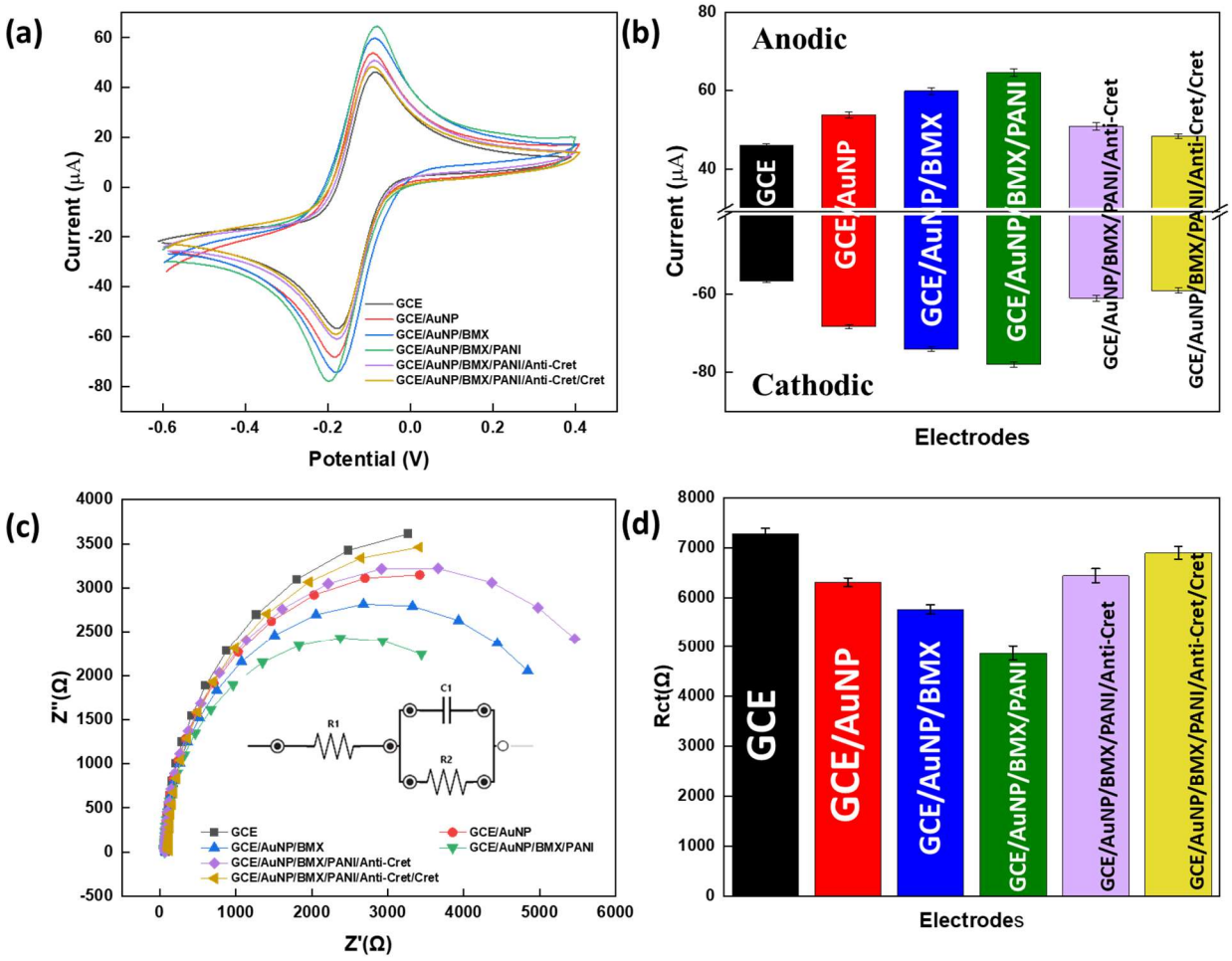

Figure 4.5: (a) *CV responses of bare GCE (black), GCE/AuNP (red), GCE/AuNP/BMX (blue), GCE/ AuNP/BMX/PANI (green), GCE/AuNP/BMX/PANI/Anti-Cret (purple), GCE/AuNP/BMX/PANI/Anti-Cret/Cret (yellow) modified electrode surfaces in 5 mM RuHex,* ***(b)*** *histogram representing anodic and cathodic current responses for each modified electrode surface,* ***(c)*** *EIS responses of GCE, GCE/AuNP, GCE/AuNP/BMX, GCE/AuNP/BMX/PANI, GCE/AuNP/BMX/PANI/Anti-Cret, GCE/AuNP/BMX/PANI/Anti-Cret/Cret modified electrode surfaces (inset: equivalent Randles circuit; where C1, R1, and R2 represents the double layer capacitance, electrolyte resistance, and charge transfer resistance, respectively),* ***(d)*** *histogram showing the respective R_{ct} values obtained from the EIS spectra*

Further, scan rate study was conducted to evaluate the process occurring at the electrode/electrolyte interface, where the CV at GCE/AuNP/BMX/PANI/Anti-Cret sensor probe were recorded by varying scan rates between 10 and 100 mV/s (**Figure 4.6(a)**). After that, the obtained peak current values from scan rate study were plotted against the square root of scan rates as shown in **Figure 4.6(b)**. The anodic (I_{pa}) and cathodic (I_{pc}) peak currents were found to be directly proportional to the square root of the scan rate, with correlation coefficients of 0.99, and 0.99, respectively. The linear relationship between square root of scan rates and current for both oxidation and reduction process clearly suggested a diffusion-controlled process at the electrolyte/electrode interface. The data also implies that the developed surface is highly stable even at higher scan rates, indicating its deployment for precise creatinine detection.

The effective surface area of electrode till antibody immobilization was calculated that helped in comparing the charge transfer and electrocatalytic activity using Randles Sevcik's model, **equation 1**:

$$\mathbf{I_p = 2.69 \times 10^5\ n^{3/2} A C D^{1/2} \nu^{1/2}} \qquad \textbf{equation 1}$$

where, I_p: peak current (A); n: number of electrons transferred in a redox reaction [in this work, n=1]; D: diffusion coefficient (cm^2/s); A: effective surface area (cm^2); C: concentration of the electroactive species ($mole/cm^3$); v: scan rate in V/s.

The calculated area was found to be 0.82, 0.86, 0.93, 1.05, 0.83 cm^2 for bare GCE, GCE/AuNP, GCE/AuNP/BMX, GCE/AuNP/BMX/PANI, and GCE/AuNP/BMX/PANI/Anti-Cret, respectively.

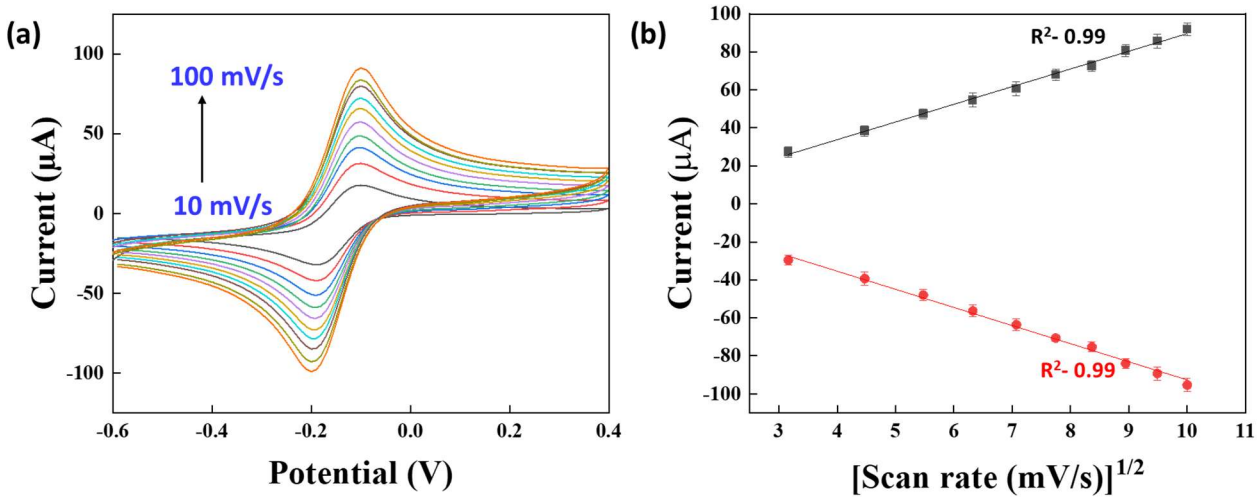

Figure 4.6: (a) *CV responses of the GCE/AuNP/BMX/PANI/Anti-Cret sensor probe at different scan rates (10 - 100 mV/s) in 5mM RuHex solution,* ***(b)*** *the corresponding linear regression for* I_{pa} *and* $I_{pc.}$

3.4 Analytical Performance

At first stage the experimental parameters affecting the analytical performance of the immunosensor were optimized in terms of antibody concentration, pH, and reaction time. The optimum concentration of antibody was found to be 10 µg/mL, however, over this concentration no signal was enhanced most likely due to the saturation effect. The pH value of 7.2 was ideal for maximum signal generation which may be due to the stability of the immobilized antibodies at this pH. Not only this, the optimized pH value is close to the pH of physiological body fluids, indicating the importance of fabricated sensor for creatinine detection in clinical samples such as serum. We also investigated the immunocomplexation time where 20 min. was found to be optimal, however over this time the signal was saturated. This is most likely due to the complete interaction between Anti-Cret and creatinine during this time span. All the experiments were performed at ambient temperature that is comparable to the standard laboratory testing temperature.

After the successful fabrication and optimization of the immunosensor (GCE/AuNP/BMX/PANI/Anti-Cret), the analytical performance was checked towards creatinine detection. The final probe was incubated with varying concentrations of creatinine from 10 nM to 0.1 M for 20 min and the current signal was measured using DPV in 5 mM RuHex. All experiments were performed in triplicates (n = 3). **Figure 4.7(a)** represents a gradual decrease in the current values with increasing creatinine concentrations. The electron transfer between RuHex and the electrode surface was hindered due to the increase in immunocomplexation on the sensor surface. The linear equation of the obtained calibration curve was represented as: ΔI (μA) = 24.63(± 1.22) $\log_{10}$[Conc.(M)] + 223.27 (±7.51), with a correlation coefficient of 0.98 (**Figure 4.7(b)**). The sensor response was highly precise within the linear dynamic range (LDR), as indicated by the small error bars.

The limit of detection (LOD) of the immunosensor was found to be 1.72 (±0.07) nM, calculated using the **equation 2**:

$$\boldsymbol{LOD = \frac{3.3\,SD}{m}} \qquad \textbf{equation 2}$$

where SD is the standard deviation of the blank sample and m represents the slope of the calibration curve.

The limit of quantification (LOQ) of the immunosensor was also calculated using the **equation 3** and was found to be 5.10 (±0.21) nM.

$$\boldsymbol{LOQ = \frac{10\,SD}{m}} \qquad \textbf{equation 3}$$

where SD is the standard deviation of the blank sample and m represents the slope of the calibration curve.

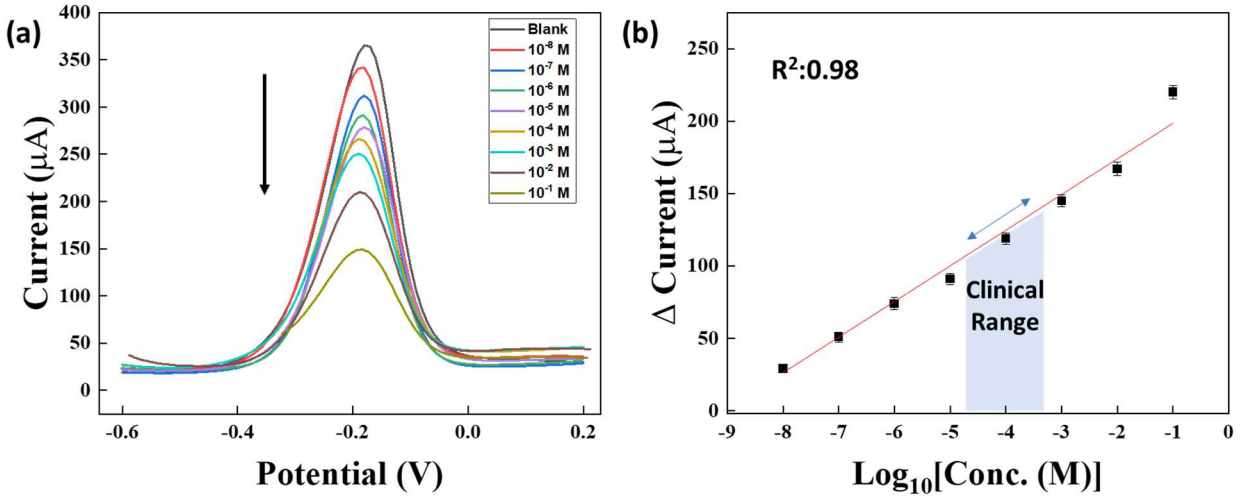

Figure 4.7: (a) *DPV responses of the GCE/AuNP/BMX/PANI/Anti-Cret sensor probe with different concentrations of creatinine (10^{-8} - 10^{-1}M) in 5 mM RuHex solution,* ***(b)*** *linear calibration curve of the response recorded with R^2 value of 0.98*

These results suggests that the fabricated immunosensor not only detect creatinine in the clinically relevant ranges but it is also able to detect its level below and beyond those concentrations. A comparative analysis showing the performance of the developed probe with the recently reported electrochemical sensors for creatinine detection has been comprehensively described in **Table 4.1**.

Table 4.1: *Comparative analysis of recently developed creatinine sensors discussing their configuration, detection technique, analytical performance, and real sample analysis (NR: Not reported).*

S. No.	Sensor Configuration	Detection Technique	Dynamic Range	LOD	Real Sample	Ref.
1.	CuNPs/Cu-MOF-199@MWCNTs/GCE	Square Wave Voltammetry (SWV)	0.05 - 40 µM	11.3 nM	Serum	[19]
2.	eCu-PMF	SWV	100 fM - 60 mM	NR	Serum	[20]
3.	SB3C16@Cu_2O-Au	DPV	10.0 - 200 µM 1.00 - 35.0 mM	0.72 µM 2.41 mM	Urine	[21]
4.	Co-Hydantoin complex	CV	0.2 - 4 mg/dL	NR	Serum	[22]
5.	Nanoporous Au/Picric Acid	CV	10 - 2000 µM	10 µM	Urine	[23]
6.	CNT/Folic acid/AgNP	DPV	0.01 - 200 µM	0.008 µM	Urine	[24]
7.	aptamer-AuNPs@ZIF-8	Electrochemical Impedance Spectroscopy (EIS)	0.1 - 1000 µM	NR	Urine	[34]
8.	GQDs/Fe3O4/Ppy/GCE	DPV	0.1 - 100 µM	0.009 µM	Serum	[35]
9.	Pd/Cu2O/PPy	DPV	0.1 - 150 µM	0.05 µM	Urine	[36]
10.	**AuNP/BMX/PANI/Anti-Cret**	**DPV**	**10 nM - 0.1 M**	**1.72 nM**	**Serum**	**This work**

3.5 Selectivity Assay

The selectivity of the fabricated immunosensor was evaluated by checking its performance in the presence of interfering molecules that co-exist with creatinine in the serum sample. Hence, numerous co-existing molecules were selected, such as glucose, glutamine, uric acid, alanine, K^+, Na^+, ascorbic acid, ALP, glutathione, ribonuclease, and albumin, to check the selectivity of the fabricated sensing probe. The DPV responses were recorded against each interfering molecule separately and the obtained change in current values were plotted in histogram (**Figure 4.8(a)**). The selectivity coefficient (K_{sel}) of the interfering molecules was calculated using **equation 4**, and the recorded values are represented in **Table 4.2.**

$$K_{sel} = \frac{(Signal)_{interferent}}{(Signal)_{Cret}} \qquad \textbf{equation 4}$$

where K_{sel} represents the selectivity coefficient, $(Signal)_{interferent}$ represent the analytical signal corresponds to interfering molecule, and $(Signal)_{Cret}$ represents the analytical signal corresponds to creatinine of the final sensing probe.

It was observed that $K_{sel} < 0.05$ which highlights good selectivity of the fabricated immunosensor towards creatinine. Using the t-test to determine the statistical significance of the results, it was discovered that the co-existing molecules' p-value against creatinine was <0.003, n = 3. We also examined the efficiency of fabricated immunosensor in terms of creatinine detection in presence of the interfering molecules i.e., mixed sample analysis.

It was interesting to note that in this case the signal generated was 96.34 % consistent (orange bar in **Figure 4.8(a)**) to those which was obtained when creatinine was analysed separately. This suggests that the immunoprobe is capable of detecting creatinine in presence of several interfering molecules.

Table 4.2: *Description of interfering molecule representing their K_{sel} and % RSD*

S. No.	Interfering molecules	Current Magnitude (µA)	% RSD	K_{sel}
1.	Glucose	4.16 (± 0.12)	2.94	0.040
2.	Glutamine	3.94 (± 0.11)	2.76	0.048
3.	Uric acid	2.57 (± 0.04)	1.36	0.031
4.	Alanine	3.95 (± 0.06)	1.50	0.048
5.	K^+	3.67 (± 0.08)	2.48	0.042
6.	Na^+	3.07 (± 0.03)	1.15	0.036
7.	Ascorbic acid	1.64 (± 0.04)	2.43	0.019
8.	ALP	2.17 (± 0.09)	4.31	0.024
9.	Glutathione	2.95 (± 0.07)	2.75	0.034
10.	Ribonuclease	4.09 (± 0.18)	4.51	0.048
11.	Albumin	3.77 (± 0.08)	2.36	0.043
12.	Creatinine	83.86 (± 1.43)	1.74	1

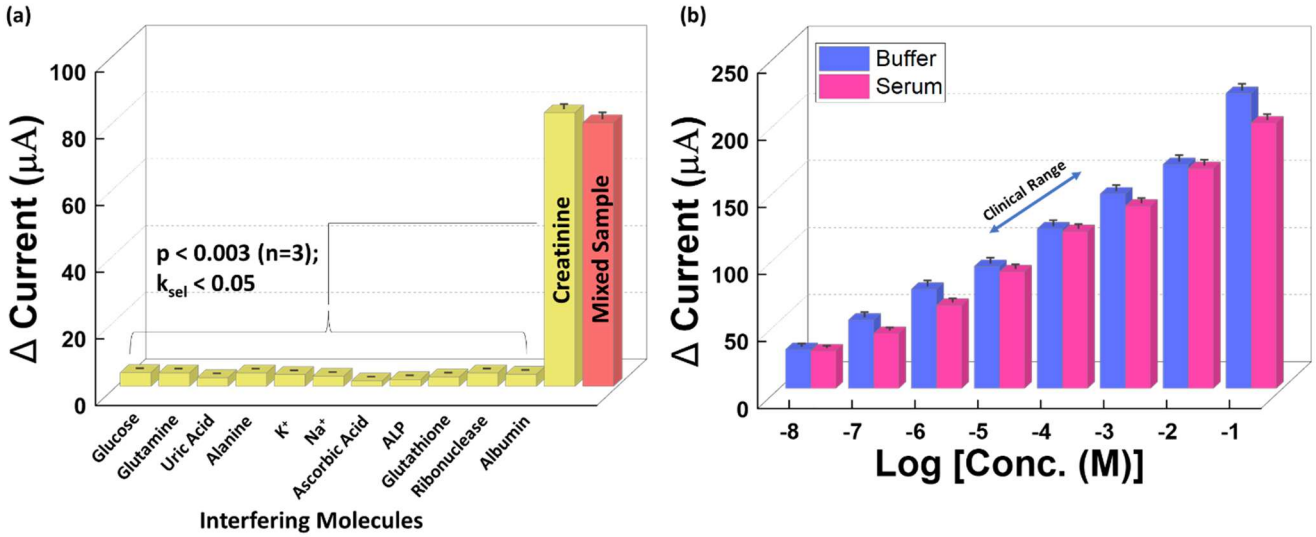

Figure 4.8: (a) *Histogram representing the selectivity assay against interfering molecules,* ***(b)*** *Histogram representing the comparative concentrations dependent responses of creatinine in final sensing probe in buffer and serum sample*

3.6 Real Sample analysis

For the commercial application, the analytical capability of fabricated sensing probe needs to be analysed in the real sample [37]. Hence, in this case, serum sample was selected as a real matrix for performing the experiment using the final GCE/AuNP/BMX/PANI/Anti-Cret sensing probe. For this, known concentrations of creatinine were spiked into the serum sample and data were recorded using fabricated probe. The percentage recovery of the final immunoprobe for different concentrations were calculated using **equation 5**.

$$\%\ \boldsymbol{Recovery} = \frac{[X]_{Cret} - [Y]_{Cret}}{[Z]_{Cret}}\ \boldsymbol{x\ 100} \qquad \textbf{equation 5}$$

where $[X]_{Cret}$ and $[Y]_{Cret}$ represents the creatinine concentrations for the spiked and blank sample respectively; $[Z]_{Cret}$ represents the creatinine concentrations using the standard buffer solution (PBS).

In this study, the concentration-dependent DPV responses showed a decrease in the current signals with increase in creatinine concentrations. The histogram in **Figure 4.8(b)** represents the change in current values obtained from concentration-dependent responses in serum and buffer samples using the sensing probe. The observed recovery percentage in serum samples for different concentrations were between 90.16 and 96.45 % with RSD < 4.9 %. The obtained calibration curve for the serum sample was represented as ΔI (μA) = 23.16(± 1.06) $\log_{10}$[Conc.(M)] + 208.55 (±6.82), with a correlation coefficient of 0.98. The LOD was found to be 4.23 (±0.18) nM based on the standard deviation of three consecutive responses of the blank. These findings indicated that the developed sensing probe was able to determine creatinine efficiently in the serum samples and thus can be employed in real world analysis.

3.7 Repeatability and Reproducibility

The developed sensor needs to be highly accurate and repeatable in order to be commercially viable [38]. To confirm the reproducibility of the GCE/AuNP/BMX/PANI/Anti-Cret sensor, the current responses were compared across five different electrodes that were developed using the same procedure. When the repeatability of the sensor was assessed, it was found that even with the similar fabrication process, the RSD was < 4.38% (n = 3) and the probe-to-probe RSD was < 5.32%. This minor variation in the signal was most likely due to some handling errors during fabrication as the probes were developed manually. Further, the long-term performance of the GCE/AuNP/BMX/PANI/Anti-Cret sensor probe was assessed at 4 °C and the results indicate that the sensor maintained 90.21% (RSD < 3.72 %) of its initial response for a period of four weeks. Further after four weeks the activity of the developed probe was further decreased.

4. Designing and Deployability of Smartphone-Integrated Sensing System

Conventionally for performing electrochemical sensing, the generated data from the potentiostat needs to be calculated manually which required skilled personnel and processing time. The data analysis from the experiment is a multi-step procedure which includes (i) plotting the current value as a calibration curve for standard solutions, (ii) interpreting the concentration using it, and (iii) testing the analyte concentrations in real samples. Hence, implementation of electrochemical system in the remote areas for performing clinical analysis becomes a challenging task. Therefore, to simply the process we need a method through which the data processing can be done directly without the need of manual interventions. For targeting this, we have developed a software called "**CretCheck**" which helps in automating the multi-step procedure and thus can be employed in primary healthcare facilities. **Figure 4.9** represents the detailed systemic workflow for the designing and development of the software for the hand-held device. The software was coded in

such a way that it can analyse the given readout provided by the sensor system and then calculate the creatinine level in different samples. The software was developed using Flutter, a framework within Visual Studio Code, and programmed primarily in the Dart language.

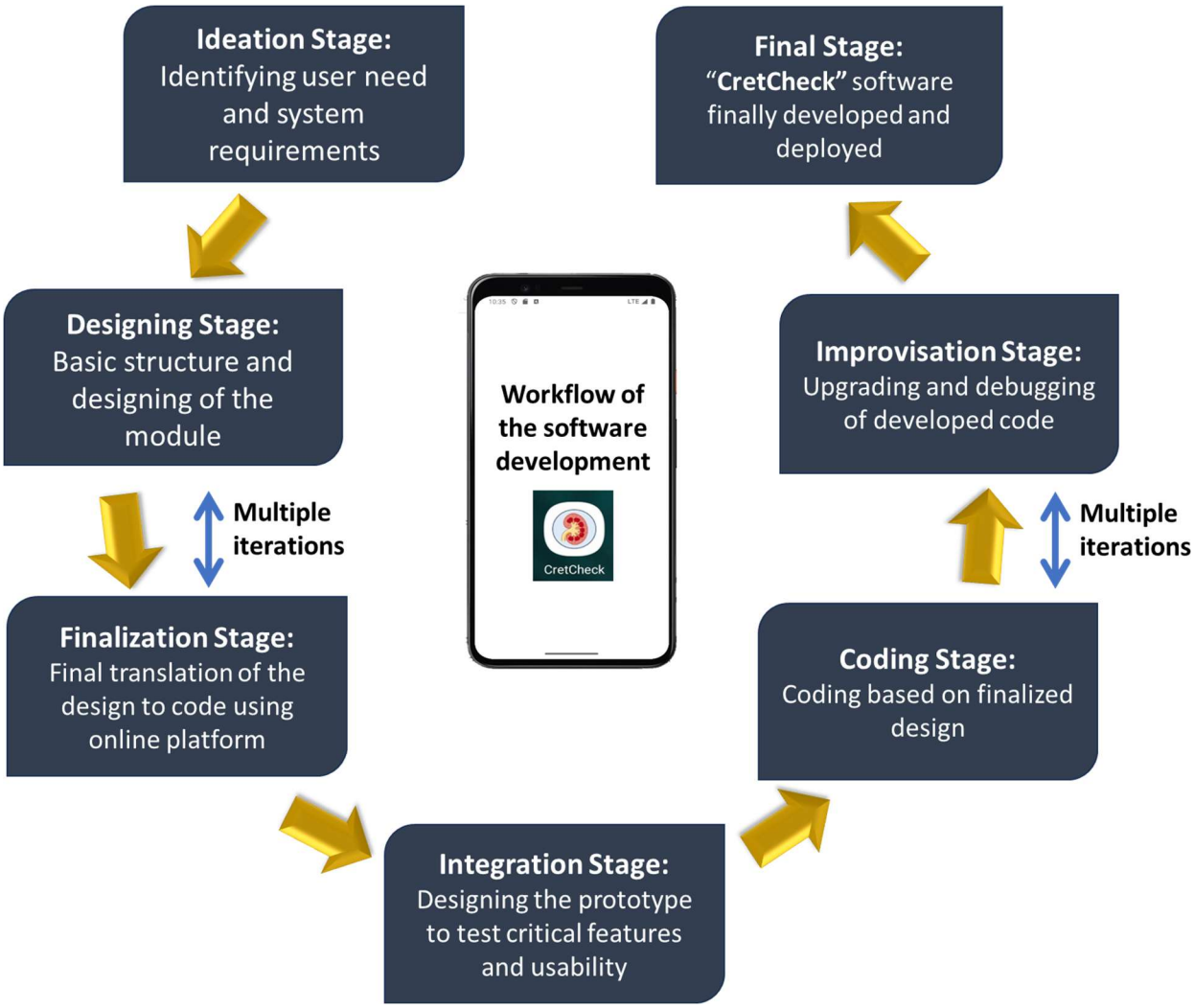

Figure 4.9: *Detailed workflow representing the different stages of the software development for creatinine biosensing starting from the ideation stage to finally developed software*

Data security is a necessary feature for the developed software where information about the patient and the result is highly sensitive in nature. "CretCheck" takes into account the need for security features to protect patient confidentiality and to protect the integrity of clinical data. Standard encryption methods help minimize the risk to patient data in a client-server architecture,

both in transit and for data at rest. The major emphasis was given to secure data storage and backup procedures that would help reduce the chances of patients not being stored properly or losing patients' records. Anonymization practices can be used particularly when there is a data sharing that needs to comply with ethical frameworks that protect a patient's identity. The architecture of the software allows for upgrades and security patches that could help defend against cyberthreats that are always coming in new forms.

Figure 4.10 represents the user interface and the images of the screens that appear in the smartphone. The first screen upon entering the smartphone interface shows two options namely 'Test Now' and 'History' (**Figure 4.10(a)**). 'Test Now' section has to be entered for performing the analysis and a space is provided there for entering the obtained current value. After this, the creatinine concentration in the sample is obtained upon clicking on the creatinine icon **(Figure 4.10(a))**. This is made feasible by the software's built-in memory, which possess the internal calibration which can be used as reference to provide the creatinine concentrations in the test sample. At the interface, the appearance of green/red colour rapidly indicate the normal or high level of creatinine in the test samples (**Figure 4.10(b,c)**). In addition, the program also saves the analysis data along with its date and day that can be visualized from the "Check History" section (**Figure 4.10(d)**). By following all the instructions, the app can be exited, returned to the home screen or even the test can be repeated.

The developed software was employed for calculating the creatinine concentrations in the linear dynamic range from the different serum samples. All these system validation experiments were performed in triplicates ($n=3$) and the obtained data was processed manually and using the CretCheck" software in separate experimental settings. The results showed 98.43% agreement in the experimental results, however, the software enable system provided the data with just a click

compared to the manual process. Not only this, it is also worth mentioning that the developed integrated system reduces manual work load and minimises human error by processing large datasets rapidly and accurately in real time. Thus, this software-integrated system can be deployed for personalised healthcare monitoring and as a highly automated system that can save and compare the large dataset, even in the resource limited settings.

The drive link containing the software coding:

https://drive.google.com/drive/folders/1-HMf8_sSQYl2d3L92SbFQX7B5v14CTXJ?usp=sharing

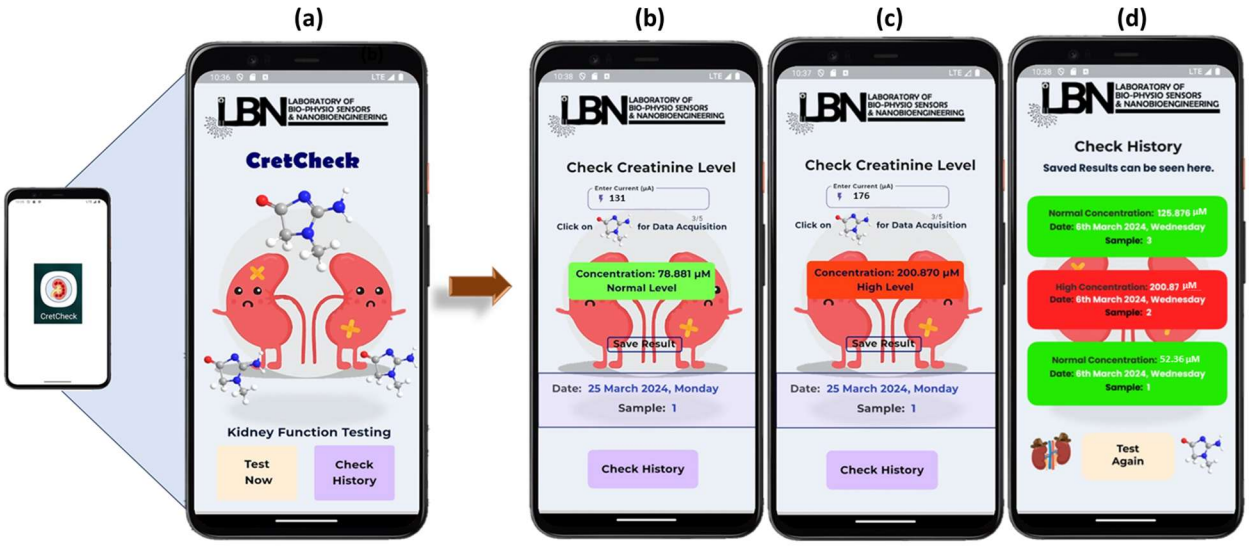

Figure 4.10: *Screenshots of the developed software* ***(a)*** *user interface after logging the software showing 'Test Now' and 'History' options,* ***(b)*** *reading of creatinine concentration in normal clinical range represented by green mark,* ***(c)*** *reading of creatinine concentration in diseased condition represented by red mark,* ***(d)*** *user interface of the check history option representing the date, time, sample name of the test and back option to go for testing again.*

5. Conclusion

In this study, we have developed a smartphone-integrated electrochemical immunosensor for the detection of creatinine in physiological fluid. The immunosensor was fabricated using the step-by-step procedure to form the final GCE/AuNP/BMX/PANI/Anti-Cret sensing surface. The fabricated sensing surface after every modification over electrode surface were characterized using SEM,

EDS, SPM, FTIR, and electrochemical techniques. The analytical performance was analysed using different concentrations of creatinine in buffer and serum samples. The developed sensor covered a wide dynamic range (10 nM - 0.1 M) including the clinically relevant concentrations, thus proving its application in the real-world analysis. We have also integrated a software to simply the process of data analysis that helps in its applicability in health care facilities of remote areas. The software is able to calculate the creatinine concentration in the sample directly by providing the analytical signals after immunocomplexation reaction. Therefore, the ability to detect creatinine in clinically relevant ranges and the incorporation of software will facilitate the application of this technology in real-world analysis.

References

[1] W.G. Couser, G. Remuzzi, S. Mendis, M. Tonelli, The contribution of chronic kidney disease to the global burden of major noncommunicable diseases, Kidney Int. 80 (2011) 1258–1270.

[2] E.F. Carney, The impact of chronic kidney disease on global health, Nat. Rev. Nephrol. 2020 165. 16 (2020) 251–251.

[3] D.E. Weiner, Public Health Consequences of Chronic Kidney Disease, Clin. Pharmacol. Ther. 86 (2009) 566.

[4] R. Burgos-Calderón, S.Á. Depine, G. Aroca-Martínez, Population Kidney Health. A New Paradigm for Chronic Kidney Disease Management, Int. J. Environ. Res. Public Health. 18 (2021) 6786.

[5] Divya, Darshna, A. Sammi, P. Chandra, Design and development of opto-electrochemical biosensing devices for diagnosing chronic kidney disease, Biotechnol. Bioeng. 120 (2023) 3116–3136.

[6] Excellence Care and Health for Institute National, Chronic kidney disease: assessment and management, Chronic Kidney Dis. Assess. Manag. 203 (2021) 1–72.

[7] R.G. Fassett, S.K. Venuthurupalli, G.C. Gobe, J.S. Coombes, M.A. Cooper, W.E. Hoy, Biomarkers in chronic kidney disease: a review, Kidney Int. 80 (2011) 806–821.

[8] C.S. Pundir, S. Yadav, A. Kumar, Creatinine sensors, TrAC Trends Anal. Chem. 50 (2013) 42–52.

[9] Divya, P. Chandra, Bioengineered cellulosic paper micro-device for serum albumin detection in clinical range, Int. J. Biol. Macromol. 258 (2024) 128921.

[10] G. del Campo, A. Irastorza, J.A. Casado, Spectrophotometric simultaneous determination

of creatinine and creatine by flow injection with reagent injection, Fresenius. J. Anal. Chem. 352 (1995) 557–561.

[11] E. Schwedhelm, D. Tsikas, T. Durand, F.M. Gutzki, A. Guy, J.C. Rossi, J.C. Frölich, Tandem mass spectrometric quantification of 8-iso-prostaglandin F2alpha and its metabolite 2,3-dinor-5,6-dihydro-8-iso-prostaglandin F2alpha in human urine, J. Chromatogr. B. Biomed. Sci. Appl. 744 (2000) 99–112.

[12] E.A. Clark, J.C. Fanguy, C.S. Henry, High-throughput multi-analyte screening for renal disease using capillary electrophoresis, J. Pharm. Biomed. Anal. 25 (2001) 795–801.

[13] C.S. Pundir, P. Kumar, R. Jaiwal, Biosensing methods for determination of creatinine: A review, Biosens. Bioelectron. 126 (2019) 707–724.

[14] V. Borse, P. Chandra, R. Srivastava, eds., BioSensing, Theranostics, and Medical Devices, BioSensing, Theranostics, Med. Devices. (2022).

[15] P. Mehrotra, Biosensors and their applications – A review, J. Oral Biol. Craniofacial Res. 6 (2016) 153.

[16] P. Chandra, R. Prakash, Nanobiomaterial engineering: Concepts and their applications in biomedicine and diagnostics, Nanobiomaterial Eng. Concepts Their Appl. Biomed. Diagnostics. (2020) 1–294.

[17] B. Purohit, P.R. Vernekar, N.P. Shetti, P. Chandra, Biosensor nanoengineering: Design, operation, and implementation for biomolecular analysis, Sensors Int. 1 (2020) 100040.

[18] Handbook of Nanobioelectrochemistry, Handb. Nanobioelectrochemistry. (2023).

[19] P. Ming, Y. Niu, Y. Liu, J. Wang, H. Lai, Q. Zhou, H. Zhai, An Electrochemical Sensor Based on Cu-MOF-199@MWCNTs Laden with CuNPs for the Sensitive Detection of Creatinine, Langmuir. 39 (2023) 13656–13667.

[20] D. Mehta, A. Kafle, T.C. Nagaiah, Flexible electrochemical sensor for highly sensitive and selective non-enzymatic detection of creatinine via electrodeposited copper over polymelamine formaldehyde, J. Mater. Chem. B. 11 (2023) 11103–11109.

[21] R.K.R. Kumar, A. Kumar, M.O. Shaikh, C.Y. Liao, C.H. Chuang, Enzymeless electrochemical biosensor platform utilizing Cu2O-Au nanohybrids for point-of-care creatinine testing in complex biological fluids, Sensors Actuators B Chem. 399 (2024) 134787.

[22] P. Dasgupta, V. Kumar, P.R. Krishnaswamy, N. Bhat, Serum creatinine electrochemical biosensor on printed electrodes using monoenzymatic pathway to 1-methylhydantoin detection, ACS Omega. 5 (2020) 22459–22464.

[23] K. Shang, S. Wang, S. Chen, X. Wang, Sensitivity Detection of Uric Acid and Creatinine in Human Urine Based on Nanoporous Gold, Biosensors. 12 (2022) 588.

[24] A.M. Fekry, S.A. Abdel-Gawad, R.H. Tammam, M.A. Zayed, An electrochemical sensor for creatinine based on carbon nanotubes/folic acid /silver nanoparticles modified electrode, Measurement. 163 (2020) 107958.

[25] R. Akhter, S.S. Maktedar, MXenes: A comprehensive review of synthesis, properties, and progress in supercapacitor applications, J. Mater. 9 (2023) 1196–1241.

[26] A. Sohan, P. Banoth, M. Aleksandrova, A. Nirmala Grace, P. Kollu, Review on MXene synthesis, properties, and recent research exploring electrode architecture for supercapacitor applications, Int. J. Energy Res. 45 (2021) 19746–19771.

[27] L. Chen, X. Dai, W. Feng, Y. Chen, Biomedical Applications of MXenes: From Nanomedicine to Biomaterials, Accounts Mater. Res. 3 (2022) 785–798.

[28] A. Nikkhah, H. Nikkhah, H. langari, A. Nouri, A. Wahab Mohammad, A. Wei Lun, N. law

Yong, R. Rohani, E. Mahmoudi, MXene: From synthesis to environment remediation, Chinese J. Chem. Eng. 61 (2023) 260–280.

[29] A. Bhat, S. Anwer, K.S. Bhat, M.I.H. Mohideen, K. Liao, A. Qurashi, Prospects challenges and stability of 2D MXenes for clean energy conversion and storage applications, Npj 2D Mater. Appl. 2021 51. 5 (2021) 1–21.

[30] R. Wang, M. Li, K. Sun, Y. Zhang, J. Li, W. Bao, R. Wang, M. Li, Y. Zhang, J. Li, W. Bao, K. Sun, Element-Doped Mxenes: Mechanism, Synthesis, and Applications, Small. 18 (2022) 2201740.

[31] A. Dey, S. Varagnolo, N.P. Power, N. Vangapally, Y. Elias, L. Damptey, B.N. Jaato, S. Gopalan, Z. Golrokhi, P. Sonar, V. Selvaraj, D. Aurbach, S. Krishnamurthy, Doped MXenes—A new paradigm in 2D systems: Synthesis, properties and applications, Prog. Mater. Sci. 139 (2023) 101166.

[32] M. Alhabeb, K. Maleski, B. Anasori, P. Lelyukh, L. Clark, S. Sin, Y. Gogotsi, Guidelines for Synthesis and Processing of Two-Dimensional Titanium Carbide (Ti3C2Tx MXene), Chem. Mater. 29 (2017) 7633–7644.

[33] V.S.P.K.S.A. Jayanthi, A.B. Das, U. Saxena, Fabrication of an immunosensor for quantitative detection of breast cancer biomarker UBE2C, RSC Adv. 9 (2019) 16738–16745.

[34] A. Ganguly, A. Paul, S. Prasad, Pysanka-Inspired Electrode Modification with Aptamer Encapsulation in ZIF-8 for Urine Creatinine Electrochemical Biosensing, Chemosensors. 11 (2023) 557.

[35] C. Bhuvaneswari, A. Elangovan, N. Sudhan, G. Vinodhkumar, S. Saravanan, V. Balasubramanian, C. Sharmila, S. Karuppaiah, A low-cost hybrid

GQDs/Fe3O4/polypyrrole nanocomposite based chemo-sensor for electrochemical non-enzymatic selective determination of creatinine in biological samples, Microchem. J. 194 (2023) 109259.

[36] A. Nagarajan, V. Sethuraman, R. Sasikumar, Non-enzymatic electrochemical detection of creatinine based on a glassy carbon electrode modified with a Pd/Cu2O decorated polypyrrole (PPy) nanocomposite: an analytical approach, Anal. Methods. 15 (2023) 1410–1421.

[37] P. Chandra, Nanobiosensors for Personalized and Onsite Biomedical Diagnosis, Institution of Engineering and Technology, 2016. https://doi.org/10.1049/PBHE001E.

[38] Immunodiagnostic Technologies from Laboratory to Point-Of-Care Testing, Immunodiagn. Technol. from Lab. to Point-Of-Care Test. (2021).